Bridging hexatic and tetratic phases in binary mixtures through near critical point fluctuations

B. P. Prajwal and Fernando A. Escobedo

Phys. Rev. Materials **5**, 024003 — Published 12 February 2021

DOI: 10.1103/PhysRevMaterials.5.024003

Bridging hexatic and tetratic phases in binary mixtures through near critical point fluctuations

B.P. Prajwal and Fernando A. Escobedo*

Department of Chemical and Biomolecular Engineering, Cornell University, Ithaca, New York 14853, USA

Abstract

Monte Carlo simulations were used to study the assembly of model binary mixtures whose pure components have either distinct or similar crystal order symmetry. Specifically, we simulated mixtures of hard disks with either squares or hexagons, where the components have size ratios that optimize their co-assembly into compositionally disordered solids. For the disks+squares mixture, along with the enhanced regions of solid miscibility, we report a novel continuous-looking transition from the disk-like to the square-like behavior that occurs through a region that seamlessly bridges the regions of hexatic phase of disks and the tetratic phase of squares, which we term the *mosaic* (M) region. For the equimolar composition, this M region is bound by the isotropic phase at low pressures and by the hexatic-tetratic (two-phase) macro-phase segregated region above a critical transition pressure. Our analysis showed that the M region lies in the vicinity of the critical point, manifesting local compositional fluctuations that give rise to micro-phase segregated regions of interspersed square-rich four-fold and rhombic lattice symmetry, and disk-rich six-fold clusters, that coexist across the system. The M behavior is characterized by a short-ranged translational order and an algebraic decay of the correlation functions for six-fold and four-fold orientational order. A finite size scaling analysis was used to evaluate the dependence of the local compositional susceptibility with the system size to extract the critical exponent associated with the approach of the critical point. For the disks+hexagons mixture, a fully mixed hexatic phase was observed for all compositions.

I. Introduction

Recent advances in the synthesis [1–3] and fabrication [4,5] of faceted sub-micron particles with different shapes have spurred interest in their use as building blocks for the assembly of targeted complex structures. Several tunable parameters like particle shape [6,7] and inter-particle interactions [7,8], allow the design of a wide range of morphologies having enhanced optical characteristics for potential applications in nanophotonics [9,10], sensing [11], and catalysis [12–14]. Towards designing such materials, recent efforts have focused on predicting phase behavior using theory [15,16] and simulation [6,17–21] for hard polyhedral particles in the bulk (3D) and in monolayers (2D), where the formation of ordered structures entirely depends on the entropic forces encoded in the particle shape. In particular, several experimental protocols leveraging slit confinement or interfacial pinning [22,23] can be deployed to assemble monolayers from different readily synthesizable nano- and micro-sized polyhedral or polygonal particles for applications in thin-film optical and electronic devices [24–28].

Single-component hard-particle superstructures arise at sufficiently high concentrations due to packing entropy manifesting as effective entropic bonds between the constituent particles. Pure systems of squares have been predicted to exhibit a Kosterlitz-Thouless-Halperin-Nelson-Young (KTHNY) [29–32] behavior, wherein the transition is continuous between both isotropic fluid and tetratic phase and tetratic and solid phases [21]. Simulation results reported for the melting behavior of hard disks suggest that the transition occurs in two steps with a first-order fluid-hexatic transition and a continuous hexatic-solid phase transition [33]. The tetratic and hexatic phases are partially ordered phases characterized by a short-range translational order and quasi-long ranged bond orientational order.

By *mixing* particles of different shapes, we can access a wider variety of superstructures having a combination of the constituents' physical properties. For example, ordered superstructures have been predicted for binary mixtures of hexagons+squares, squares+triangles, hexagons+triangles with and without enthalpic patchiness encoded in their facets [34]. The phase behavior of binary mixtures strongly depends on the relative size ratios and contents of the components. This correlation was observed, e.g, in a size-bidisperse system of hard disks, where the liquid-hexatic-solid transition changes to a first order liquid-solid transition upon increasing the composition of the small disks [35]. For binary mixtures of parallel hard squares having disparate sizes, a fluid-

solid phase-separated state was found with small and large squares forming the fluid and solid phases, respectively [36]. These predicted phase transitions reflect the interplay of mixing and packing entropy. At very high pressures, packing entropy dominates over mixing entropy leading to strong segregation of the components into their respective stable structures, separated by an interface. An interesting attribute associated with the phase separation of mixtures is the occurrence of critical behavior, the point where the two phases converge to become a single phase; this critical point can be approached either from the single or the two-phase region. The critical behavior associated with phase transitions is driven by the divergence in the magnitude of (otherwise local) compositional or density fluctuations as the critical point is approached. Critical phenomenon has been observed in a wide range of systems like colloid-polymer mixtures [37,38], active and passive colloid mixtures [39,40], and also in biophysical systems such as multi-component lipid bi-layers, and lipid monolayers [41,42].

In the context of a fundamental understanding of crystalline and partial ordering in 2D systems, the assembly of micro- and nanoparticles on hexagonal and square-lattice arrays [21,43] is well established and has been widely studied; however, much less is known about whether and how a system can be designed to gradually bridge these two types of ubiquitous lattice symmetries. In this work, we tackle this question by studying the entropy-driven assembly of binary mixtures of hard disks with squares using Monte Carlo simulations, where the components have size ratios that optimize their co-assembly into compositionally disordered solids. For reference, we also studied mixtures of disks and hexagons which, in contrast to disks and squares, exhibit pure-component solid phases and partially ordered phases with similar hexagonal lattice symmetry.

The disks+squares mixture with optimized size ratio was found to exhibit broad ranges of compositions where crystalline (with hexagonal and square order) and partially ordered phases (with hexatic and tetratic order) exist. Around the equimolar composition, a novel mosaic (M) region was observed having locally ordered microscopic clusters with square-rich four-fold and rhombic (RB) lattice symmetry, and disk-rich six-fold symmetry, that are distributed randomly throughout the simulated domain. The microscopic ordering of the four-fold and six-fold domains found in the M region are associated with the local compositional fluctuations that occur in the region closer to the hexatic-tetratic critical point. This coexistence of finite clusters of two different symmetries over a finite range of conditions (pressures and compositions) can be seen as a small

region that lies in the vicinity of the critical point, associated with the interplay of the hexatic and tetratic phases observed for the disk-rich and square-rich systems, respectively. For the binary mixtures of hexagons and disks, the hexatic phase is observed for all compositions since the individual pure-components have similar order-disorder transition behavior and lattice symmetry.

II. METHODS

A. Exchange free energy calculation

We explored the phase behavior of 2D hard binary mixtures of disks+squares and disks+hexagons, when the components have size ratios that optimize their co-assembly into solid solutions. The size ratio is defined as $\xi = \sigma/a$ where σ = disk diameter and a = polygon edge length. For this purpose, we adopted the exchange free-energy method [44] to predict ξ values which tend to maximize the range of compositions and packing fractions where substitutionally disordered solid solutions occur. This general approach was recently introduced and applied to 3D mixtures of spheres and polyhedra. The method is based on finding the ξ value that minimizes an exchange free-energy (ΔF_x) metric, which is obtained by adding the excess chemical potentials associated with substituting one particle in each pure host solid by a guest particle:

$$\Delta F_x = \mu_{ex}^{s_1}(host \rightarrow guest) + \mu_{ex}^{s_2}(host \rightarrow guest) \quad (1)$$

where $\mu_{ex}^{s_i}$ is the reduced excess chemical potential (in units of thermal energy) associated with a single-particle host-to-guest mutation in pure host phase s_i (i = 1 or 2). $\mu_{ex}^{s_i}$ is also a mixing free energy at infinite guest dilution (see connection in Supplementary Information, SI, Sec. I) and hence by minimizing ΔF_x i.e., the *"cost"* for host-guest substitutions in both solid phases, mixing entropy and substitutionally disordered solution behavior are enhanced.

ΔF_x was found by using the unoptimized Bennett's formula, resulting in,

$$\Delta F_x \approx -\ln\left\{\frac{\langle P_{acc}^{s_1}(1\rightarrow 2)\rangle}{\langle P_{acc}^{s_1}(2\rightarrow 1)\rangle}\frac{\langle P_{acc}^{s_2}(2\rightarrow 1)\rangle}{\langle P_{acc}^{s_2}(1\rightarrow 2)\rangle}\right\}, \quad (2)$$

where $\langle P_{acc}^{s_i}(i \rightarrow j)\rangle$ (or $\langle P_{acc}^{s_i}(j \rightarrow i)\rangle$) is the average acceptance probability of virtually mutating one particle of type i (or j) into a particle of type j (or i) in phase s_i at pressure, p_m [44]. p_m is the

smallest pressure at which both pure components are solid phases for a given ξ. To estimate the p_m value, we selected the isotropic→tetratic transition as the relevant condition for the squares since the tetratic phase is a partially *"ordered"* phase that is stable for a broad range of densities (see SI Sec. II). In the case of disks and hexagons, since the hexatic phase region is narrow and heterogeneous, we choose the conditions for the hexatic→triangular solid (1Δ) phase transition (had we chosen the isotropic-hexatic transition pressure instead would have made no difference). To compute ΔF_x for different ξ, we used system sizes of 5040 particles for the disks+squares system and 6400 particles for the disks+hexagons system. Figure 1a shows the results for ΔF_x vs. ξ for the hard-core mixture of disks+squares. The minimum of ΔF_x occurs for $\xi = 1.04$, which, coincidentally corresponds to ξ where the pure disks and pure squares have equivalent order-disorder transition pressure (ODP) [45]. A relatively flat profile is observed for ΔF_x between $\xi \approx 1.04$ and $\xi \approx 1.2$ (noting that $\xi \approx 1.13$ corresponds to the shapes having equal area), with differences $< 0.2\ k_bT$. This region occurs when the product of the exchange probabilities, shown in the inset of Fig. 1a, are maximized. We choose $\xi = 1.1$ as the representative optimal value expected to promote the formation of regions with substitutionally disordered solid solutions (i.e., for the disk-rich and square-rich solid solutions), being quite near to $\xi = 1.04$ at the ΔF_x minimum. Similar calculations were performed for the disks+hexagons mixture shown in Fig. 1b. We observed the ΔF_x minimum for $\xi = 1.82$ (corresponding to equal-area shapes and quite close to $\xi = 1.84$ prescribed by the equal-ODP rule [45]). The difference in ΔF_x values is $< 0.6\ k_bT$ for $1.6 < \xi < 2.0$, indicating a relatively wide range of ξ expected to promote substitutionally disordered solid solutions.

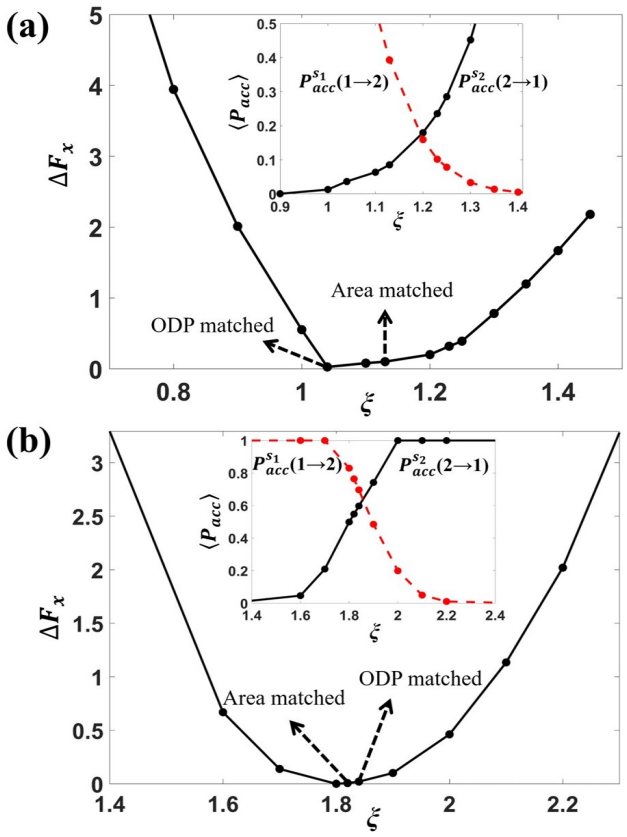

Fig. 1 (color online). Variation of the exchange free energy, ΔF_x, with component size ratio, $\xi = \sigma/a$, for the hard-core mixture of (a) disks and squares and (b) disks and hexagons (σ = diameter of disk, a = polygon edge length). The ξ values corresponding to equal footprint area and equal order-disorder transition pressure (ODP) are indicated. Curves are shifted so that the minimal value corresponds to $\Delta F_x = 0$. The inset shows the average exchange probabilities P_{acc} for mutating a host particle into a guest particle in the two solid phases (s_1-disks (1), s_2- squares or hexagons (2)) which are used to estimate ΔF_x.

B. Bond orientational order parameter

For 2D monolayer structures, the local n-fold bond orientational order, $\Phi_n(\boldsymbol{r_k})$ for each k particle is given by,

$$\Phi_n(\boldsymbol{r_k}) = \frac{1}{N_k} \sum_{j=1}^{k} \exp(in\theta_{jk}) \qquad (3)$$

Where i is the imaginary number and θ_{jk} is the angle between the vector connecting particle k with its neighbor j and a fixed reference vector. N_k is the number of nearest neighbors of particles k. For n= 6, N_k was calculated *via* Voronoi tessellation, while for n= 4, the four closest neighbors

were used to avoid the degeneracy in the Voronoi construction [46]. The global six-fold and four-fold bond order parameter is then obtained by,

$$\langle \Psi_n \rangle = \langle \frac{1}{N} \sum_{k=1}^{N} \Phi_n(\boldsymbol{r_k}) \rangle \quad (4)$$

To analyze the correlation length of the local bond order parameters, we compute the *n*-fold local bond orientational correlation function given by,

$$g_n(r^*) = \langle \Phi_n(0)\, \Phi_n^*(\boldsymbol{r}) \rangle \quad (5)$$

where * indicates the complex conjugate of $\Phi_n(\boldsymbol{r})$ for the particle at a distance $\boldsymbol{r}$ from the reference particle.

C. Mapping of pressure-composition phase diagram

At each selected composition of a mixture, we used hard-particle Monte Carlo (MC) simulations in the isothermal-isobaric *NPT* ensemble and serial compression runs with small pressure steps, $\Delta P^* = 0.4$, starting from a low-density disordered state. We simulated systems with sizes in the range $8000 \leq N \leq 11203$ to estimate equation of state data and approximate phase boundaries; e.g., for the hexatic and tetratic phases. Each pressure step entailed 10^7 MC cycles with the last 2.5×10^6 cycles used for analysis, where each cycle includes *N* translations, *N* rotations, *N*/2 swaps and 2 volume moves. A swap move randomly chooses a particle pair of different species (disk and polygon) and swap their positions while preserving the orientation of the polygon. Swap moves are imperative to speed-up the equilibration of the systems allowing particles to explore phase space far from their original positions [47]. All trial moves were accepted according to the Metropolis criterion, rejecting any overlaps between two disks, two polygons (via Gilbert-Johnson-Keerthi algorithm [48]) or a disk and a polygon (via the separating axes theorem [49]). The step size for the translational, rotational and volume moves are tuned to target acceptance probability values of 0.4, 0.4, 0.3, respectively.

We verified the formation of solid solutions by mapping the pressure-composition phase diagram for the binary mixtures with the *optimized* components size ratio ξ values (1.1 for disks+squares and 1.82 for disks+hexagons mixtures). The phase boundaries were identified by analyzing the

local correlation of the six-fold and four-fold bond-orientational (see Sec. II B for details) and the positional order parameters.

At high pressures, the disks+squares mixture phase-separate into their respective nearly pure component solid phases. The regions where the two phases coexist were mapped based on the results from interfacial simulations (see SI Sec. III). Most interfacial simulations were carried out at the equimolar global composition, with additional runs performed for other compositions to better map out the two-phase coexistence boundaries. Results are reported in dimensionless quantities for distance, $r^* = r/a$, reduced pressure, $P^* = Pa^2/k_bT$ and area fraction/density, $\eta = NA_p/A$, where P is pressure, k_b is Boltzmann's constant, T is temperature, N is the total number for particles, A is the total area of the system, and A_p is the area occupied by the particles.

D. Analysis of critical and near critical point behavior in disks+squares system

Finite size scaling (fss) analysis was used to locate the critical point and extract the critical exponents associated with the hexatic-tetratic phase transition. As the critical point is approached in the Ising model, the correlation length of the ordered domain and the local compositional susceptibility, χ, both diverge following a power law. The fss analysis provides a way to extrapolate the diverging properties obtained in finite box size simulation to the thermodynamic limit. In this study, we carry out the fss analysis for the squares+disks mixture with ξ= 1.1 to obtain the critical point and extract the critical exponents at the equimolar composition. The analysis is done for N= 10000 particles and at each value of P^*, the square simulation box with side length, L_b is divided into $N_b \times N_b$ (where N_b=1, 2,…) sub-cells of linear dimension, L (= L_b/N_b) [50]. We note here that the fluctuation observed in L at each P^* due to area-changing moves was less than 1%. We measure the χ as a function of P^* for each sub-cell width L, using the fluctuation relation given by [40],

$$\chi(P^*) = L^2 \langle (S - \langle S \rangle)^2 \rangle \qquad (6)$$

where the local order parameter, $S = x_{sq}^L - x_d^L$, x_{sq}^L and x_d^L are the compositions of squares and disks within the sub-cell of width L. The χ for the bimodal distribution observed in the two-phase region is evaluated by assuming a mixture model of two normal distributions [40]. We note here that the local compositional fluctuations gauged using the fss analysis are akin to those that would be observed in a grand canonical ensemble. The sub-cell sizes are carefully chosen such that the

length L, assuming $L \geq \mathcal{E}$ (where $\mathcal{E}$ is the correlation length), provides a reasonable statistical measure of the local compositional fluctuations.

We also performed large scale simulation in the M region that occurs near the critical point to obtain the long-ranged characteristics of the six-fold and four-fold bond-orientational order parameters. To achieve this, we followed the scale-up protocol described in Ref. [21]. First, we equilibrated the equimolar disks+squares mixture with $\xi = 1.1$ and $N = 6400$ particles in the *NPT* ensemble at $P^* = 14.9$ starting from a random initial particle configuration in a square box. The final equilibrated structure with the target density is replicated 2×2 times to obtain the initial configuration with $N = 25{,}600$ particles for the second equilibration run in the isochoric (*NVT*) ensemble. In the final stage, the equilibrated structure is again replicated to reach the target system size with $N = 102{,}400$ particles and equilibrated in the *NVT* ensemble. At every stage, the equilibration runs were carried out for 10^7 MC cycles. Results are reported in dimensionless quantities for distance, $r^* = r/a$, reduced pressure, $P^* = Pa^2/k_bT$ and area fraction/density, $\eta = NA_p/A$, where P is pressure, k_b is Boltzmann's constant, T is temperature, N is the total number for particles, A is the total area of the system, and A_p is the area occupied by the particles.

III. RESULTS AND DISCUSSION

The area fraction-composition and pressure-composition (Figs. 2a and b) phase diagrams exhibit broad stable regions of substitutionally disordered square-rich 1□ (square lattice) and disk-rich 1Δ (triangular lattice) solid solutions along with the hexatic (in disk-rich region) and tetratic (in square-rich region) phases. The disk-rich 1Δ solid phase dissolves up to 30% of squares which do not have any orientational preference and are randomly distributed throughout the underlying 1Δ lattice sites (Fig. S3 in SI Sec. V). In the square-rich side, the 1□ solid phase dissolves up to 26% of disks and is preceded by regions of tetratic and I (isotropic) phases at lower pressures. For $\eta < 0.836$ and $P^* < 19$ and for all x_s values, we observed two main phase transitions: I → hexatic and hexatic → 1Δ solid in the disk-rich region ($x_s < 0.3$) and I → tetratic and tetratic → 1□ solid in the square-rich region ($x_s > 0.74$). The transitions from the I phase to the ordered 1Δ (or 1□) solid, occurring through an intermediate hexatic (or tetratic) phase are analogous to the well-studied

phase transitions in the systems of pure monodisperse hard-disks (or hard-squares). The tetratic phase formed by the pure squares (x_s=1.0) is stable over a range ~ 8.25 < P^* < 15.4 and 0.72 < η < 0.832 [21] that is wider than the 7.59 < P^* < 7.68 and 0.716 < η < 0.72 [33,51] range of the hexatic phase formed by pure disks (x_s=0), a difference that can be attributed to the defects being more delocalized in the tetratic phase [21].

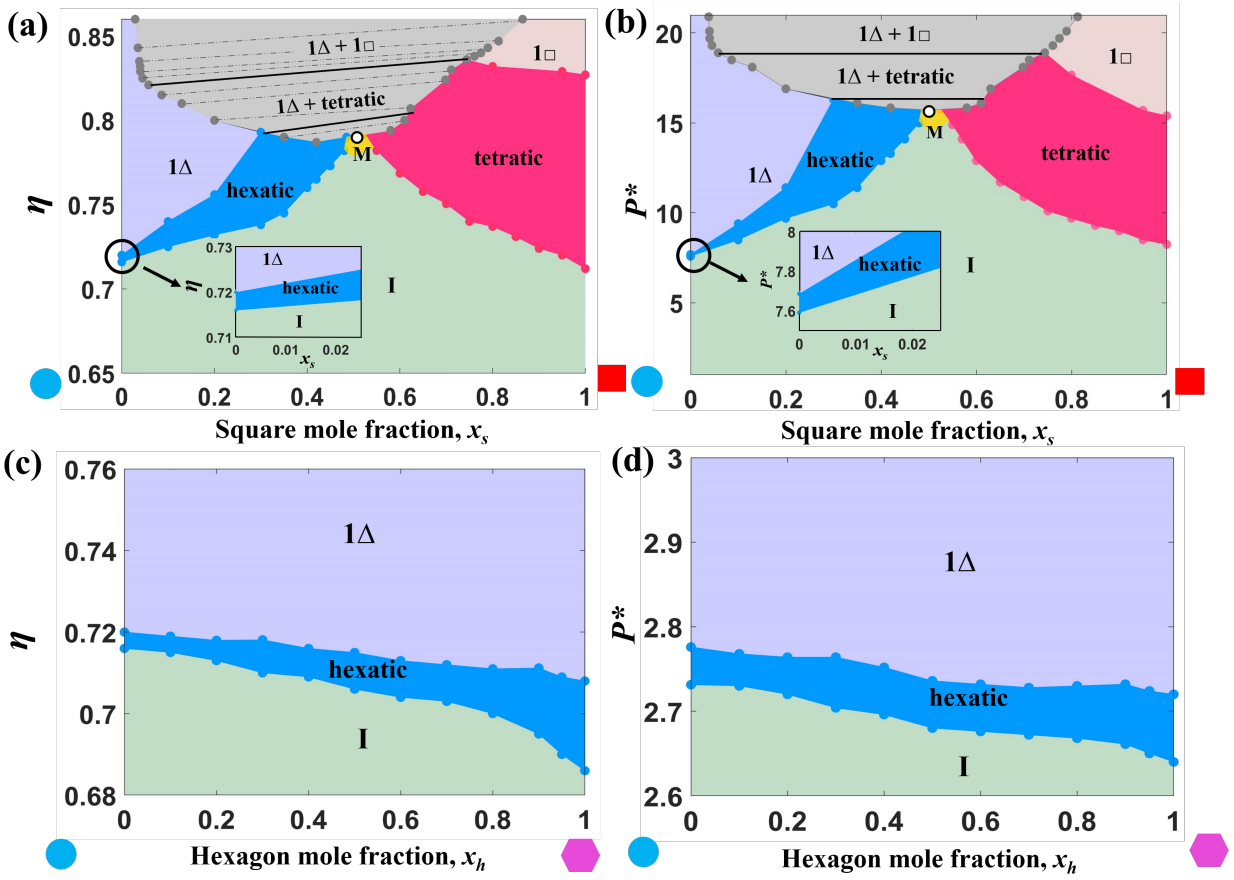

FIG. 2 (color online). Area-composition and pressure-composition phase diagram for mixtures of disks+squares (a and b) and disks+hexagons (b and c) at their corresponding optimal component size-ratio $\xi = \sigma/a$ of 1.1 and 1.82, respectively. In (a) and (b) the white dot indicates the critical point at equimolar composition and the yellow and grey-shaded area corresponds to the M region and two-phase coexistence region, respectively. In (a) the tie lines in the two-phase regions are shown as dashed lines. The insets in (a) and (b) shows the I, hexatic and 1Δ regions as $x_s \to 0$. The symbols 1Δ, 1□, and I denote the triangular solid, square solid, isotropic phase, respectively and M indicates the mosaic region.

Figure 2a and b also shows that, with increasing molar fraction of squares (disks) in the disk-rich (square-rich) region, the range of η and P^* where the hexatic (tetratic) phase is stable increases

significantly compared to the pure disk (square) system. This increase in the stability region for the hexatic phase with x_s suggests that the squares accentuate the hexatic behavior as it persists even for up to $P^* \sim 16.2$, which is approximately twice the pure-disk hexatic → 1Δ solid transition pressure of $P^* \approx 7.68$. The tetratic phase is stable up to $P^* \approx 18.9$ with increasing disk concentration, which is about 1.2 times the pure-square tetratic → 1□ solid transition pressure, $P^* \approx 15.4$. This increase in the stability regions of the hexatic and tetratic phases with the content of the guest component is attributable to the increased concentration of topological defects created by the dissimilarly shaped particles residing in the host-solid lattice. These defects tend to destroy the quasi-long-range positional correlation in the solid phases in favor of the corresponding partially ordered phases.

The disks and hexagons form a *'compatible'* mixture system since both pure components form the hexatic and 1Δ ordered phases. As shown in Figs. 2c and d, this enables a high mixing affinity that leads to the formation of a 1Δ solid solution for the entire range of hexagon compositions, x_h. The hexatic phase was stable for all compositions within the narrow range of $2.70 < P^* < 2.77$ and $0.708 < \eta < 0.72$ in the disk-rich and $2.64 < P^* < 2.73$ and $0.68 < \eta < 0.71$ in the hexagon-rich regions. We identified the boundaries between the hexatic phase and 1Δ solid solution by analyzing the positional pair-correlation and six-fold bond orientational correlation functions (see Sec. VIII and Fig. S14 in the SI for details). We note that two-1Δ phase-separated states are likely to occur at pressures much larger than those simulated here, and reach conditions where packing entropy would overtake the mixing entropy that favored the 1Δ solid-solution state. Note that for the pure disk limit in the disks+squares and disks+hexagons diagrams shown in Figs. 2b and 2d, the stability P^*-range of the hexatic phase is numerically different because P^* values are reduced with respect to the corresponding polygon edge lengths (i.e., $P^* = Pa^2/k_bT$), rather than the disk diameter. The rest of this section is devoted to analyzing the highly non-trivial results of the disks+squares mixture only.

Figures 2a and b show a peculiar continuous transition between the disk-like and the square-like behaviors over a range of square molar fractions, $0.48 < x_s < 0.53$, $14.5 < P^* < 15.72$ and $0.779 < \eta < 0.791$. We designate this region bridging the hexatic, tetratic, and isotropic phases as the mosaic (M) region. Along increasing P^* or η at the equimolar mixture composition, the M region is sandwiched between the I and (hexatic-tetratic) two-phase regions and precedes the critical point

(see Fig. 3a). Entering from the I phase, the M character in local conformations ensues at P^*= 14.5 and $\eta \approx 0.779$. As the critical point is reached at P^*= 15.72 and η= 0.791 from the M region, we observed that the distribution width of the local order parameter, S (see Fig. 3b) increases, indicating that the fluctuations of the local composition grow giving rise to the micro-domains of square-rich tetratic and disk-rich hexatic phases. At P^*= 15.84 and η= 0.793, the distribution of S changes from unimodal to bimodal indicating the onset of a two-phase coexistence state containing macro-segregated six and four-fold ordered domains within the given simulation box size. We used this incipient bimodal state (for the equimolar system at P^*= 15.84) to estimate the approximate x_s values of the two coexistence phases near the lower bound of the two-phase coexistence boundary shown in Figs. 2a and b. We expect a relatively flat boundary closer to the mixture critical point where the composition of the two coexisting phases converge.

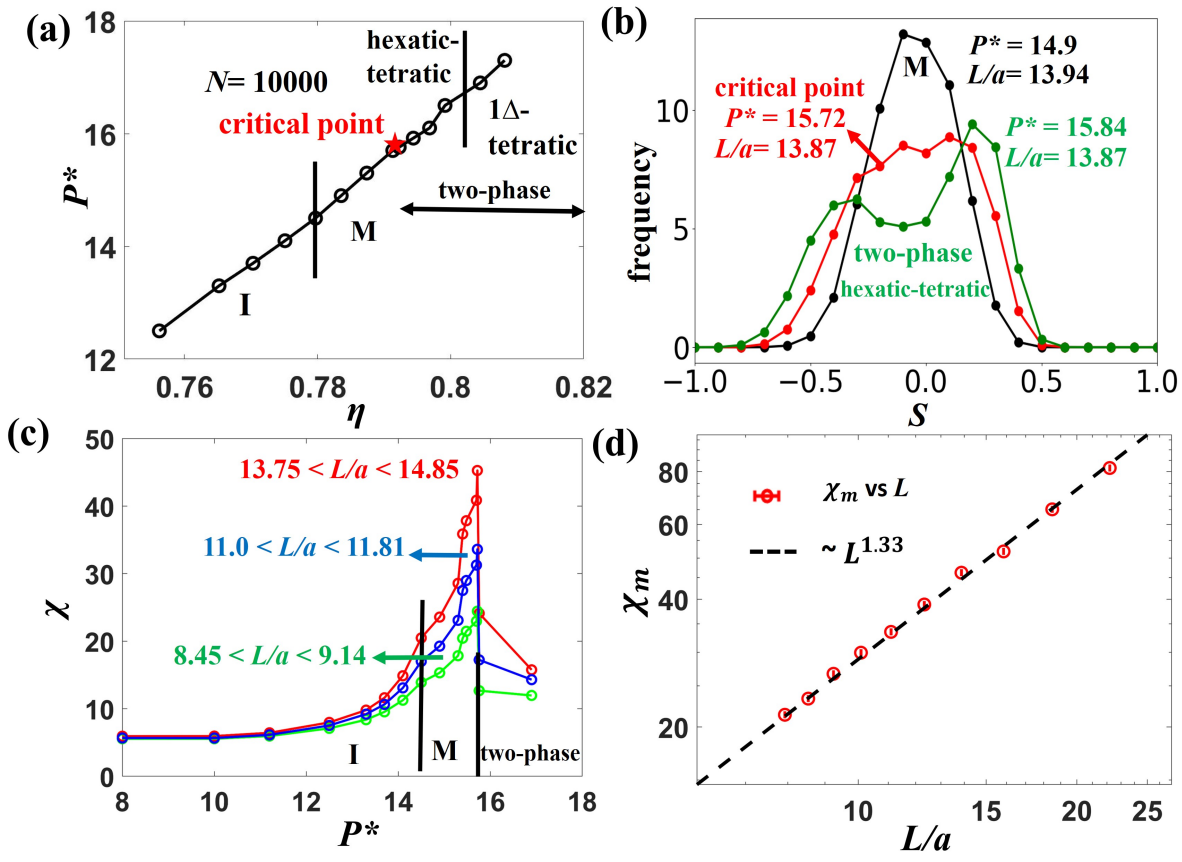

FIG. 3 (color online). Critical behavior of the equimolar disks+squares mixture with ξ = 1.1 and N = 10000. (a) Equation of state, P^* vs. η; the star marks the critical point at P^*= 15.72 and η= 0.791 and the vertical solid lines mark approximate boundaries between the I phase-M region and (hexatic-tetratic)-(1Δ-tetratic) two-phase regions. (b) Distribution of the local order parameter, S

for states along the M→hexatic-tetratic two-phase region pathway, obtained by using 8×8 sub-cells (of dimension L). (c) Local compositional susceptibility, χ, measured as a function of P^* for different sub-cell lengths, L. Approximate phase boundaries are shown. (d) Relation between the maximum local compositional susceptibility, χ_m, and L on a logarithmic scale. The error bar indicates the fluctuations observed in L and the dashed line is a fit with the critical exponent value, $\frac{\gamma}{\upsilon} = 1.33$. I = isotropic phase, M = mosaic region and a = square side length.

The critical point shown in Fig. 3a was estimated as follows. Using fss analysis, we measured the local compositional susceptibility, χ [see Eq. (6)] for different system sizes to gauge the local compositional fluctuation as shown in Fig. 3c and observed that the χ value diverges as the critical point is approached from either the M region or the two-phase region. Movie 1 in SI shows a sample simulation at the estimated critical point. The criteria for identifying the square-rich tetratic (red) and disk-rich hexatic (blue) phases in Movie 1 are discussed in Sec. VI and Fig. S8 in the SI. We quantitatively evaluate the dependence of the maximum local compositional susceptibility, χ_m with the sub-cell size, L as shown in Fig. 3d and estimated the critical exponent $\frac{\gamma}{\upsilon} = 1.33 \pm 0.01$ by using the scaling relation, $\chi_m \propto L^{\frac{\gamma}{\upsilon}}$. The power-law scaling nature of the local compositional susceptibility with the system size observed at the critical point reflects that the I→M→ (hexatic-tetratic) two-phase behavior is consistent with the continuous phase transition having critical exponents belonging to the Ising universality class. The $\frac{\gamma}{\upsilon}$ value, however, is inconsistent with the two-dimensional Ising universality class ($\frac{\gamma}{\upsilon}$=1.75), a difference that could reflect the nature of hexatic and tetratic phases at coexistence. However, at least part of this deviation can also be attributed to some of the limitations of our computational approach, e.g., the moderate range of sub-cell size, L used in our analysis. While much larger L values can allow detection of longer-range correlations of the composition within the sub-cells, much longer runs and specialized moves would be required to address the critical slowing down behavior that ensues as the critical point is approached. While our analysis is based on the variations of a single order parameter (S), field mixing with a second order parameter into an ordering operator (via suitably chosen nonuniversal scaling factors) may allow matching to the universal Ising distribution of the ordering operator at criticality [52–54];such an approach, however, would require simulations in a semigrand isobaric ensemble to allow extensive sampling of global density and composition fluctuations in a finite-size system [55–57]. Further investigation into studying the phase transition behaviors using the

classical XY spin model systems could also provide additional insights on characteristics of the system as the critical point is approached [58].

The near-critical point fluctuations of the local composition observed in the M region engenders distinctive local structural properties. To characterize and distinguish the M region from the hexatic and tetratic phases, we examined the six and four-fold local bond-orientational correlation functions, $g_6(r^*)$ and $g_4(r^*)$ [defined in Eq. (5)] and the pair correlation function, $g(r^*)$ (see Fig. 4) for x_s= 0.5. At P^*= 14.9 and η = 0.783, the M region showed algebraic decay of both $g_6(r^*)$ and $g_4(r^*)$ with an exponent value < $-¼$, and short-range layering (liquid-like behavior) of $g(r^*)$. We selected the $-¼$ exponent value as threshold to align with the KTHNY theory prediction for the scaling parameter lower-bound for the fluid to (n-fold)-atic phase transition (where n= 4 or 6). Configurations from the M region exhibit a long-ranged $g_6(r^*)$ and $g_4(r^*)$ orientational order compared to the I phase at P^*= 13.7 and η= 0.770, where we observed a quick decay in the $g_6(r^*)$ and $g_4(r^*)$ peaks. For M configurations the large-r behavior of the $g_6(r^*)$ and $g_4(r^*)$ shows algebraic decay exponents that lie within the range ~ -0.4 < η_6 < -0.25 and -0.55 < η_4 < -0.25, respectively; whereas for the I phase $g_4(r^*)$ decays exponentially and $g_6(r^*)$ decays algebraically with η_6= -0.6 (see Fig. 4c). The six-fold ordering is stronger than the four-fold ordering in the M region due to the contribution from the RB clusters in the square-rich regions. This continuous change in the correlation of the $g_6(r^*)$ and $g_4(r^*)$ orientational order as we enter the M region from the I phase signals a significant change in the size of the network of six and four-fold clusters, which correlates with the sharp growth of χ as the M region is crossed (*en route* to the critical point) for all sub-cell sizes, L (Fig. 3c). This leads to the formation of ordered micro-domains with both hexagonal-like and square-like structural motifs suggesting that the disks and squares have comparable proclivity to form stable six-fold and four-fold connections, respectively, that coexist across the system. Figure 5 shows that the algebraic decay of $g_6(r^*)$ and $g_4(r^*)$ orientational order ofM region configurations is sustained even for a larger system size, a result that correlates with the observation that χ increases with sub-cell size, L (see Fig. S12 in SI), indicative that the local compositional fluctuations of the M region increase with system size. The M character was also observed for x_s=0.49 and 0.52 (see Sec. VI Fig. S10 in SI). As we approached the disk-rich (or the square-rich) region, we observed the hexatic (or tetratic) phase with quasi-long ranged $g_6(r^*)$ (or $g_4(r^*)$) orientational order (see Fig. 2a and b). Results similar to those in Fig. 4 are shown in Fig.

S11 for the transitions I → hexatic at x_s= 0.45 and I → tetratic at x_s= 0.55. Although the M region was observed within a narrow x_s range between 0.48 and 0.53, M-like characteristics were also detectable for the hexatic (or tetratic) phase region at x_s= 0.45 (or 0.55) and P^* > 15.3 (or P^* > 14.9) where both $g_6(r^*)$ and $g_4(r^*)$ orientational order functions decay algebraically along with large values of χ (see SI Fig. S11).

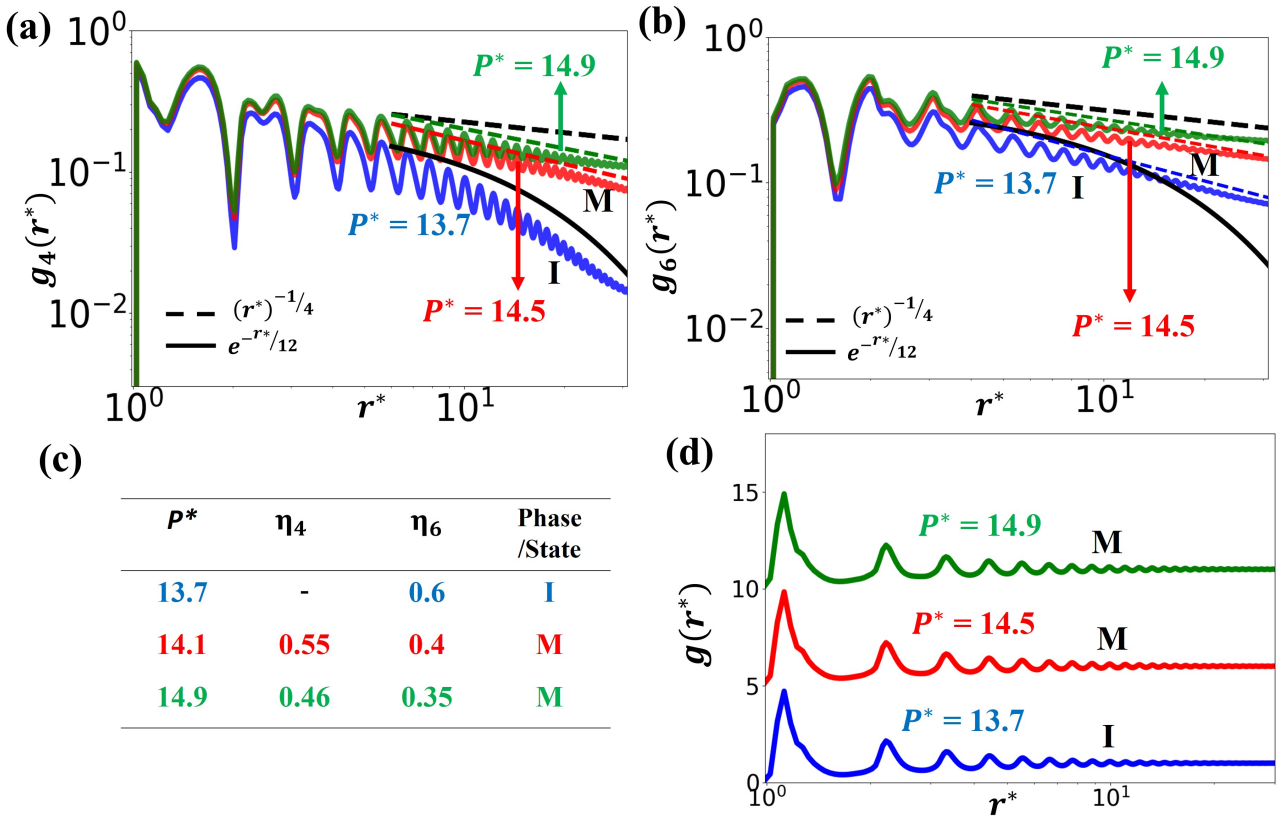

P^*	η_4	η_6	Phase /State
13.7	-	0.6	I
14.1	0.55	0.4	M
14.9	0.46	0.35	M

FIG. 4 (online color). Selected properties of equimolar disks+squares mixture with ξ = 1.1 and N = 10000. (a, b) Bond orientational order correlation functions for the I phase and the M region: $g_4(r^*)$ (a) and $g_6(r^*)$ (b). The black dashed and solid lines indicate algebraic and exponential decay of the orientational correlation with exponent $-1/4$ and $-1/12$, respectively. The algebraic decay exponent values η_4 and η_6 corresponding to the green and blue dashed lines shown in (a and b) for the I phase and M region are reported in table (c). (d) 2D pair correlation functions shifted uniformly to distinguish peaks for the phases and conditions indicated (by pressures P^*). I = isotropic phase, M = mosaic region.

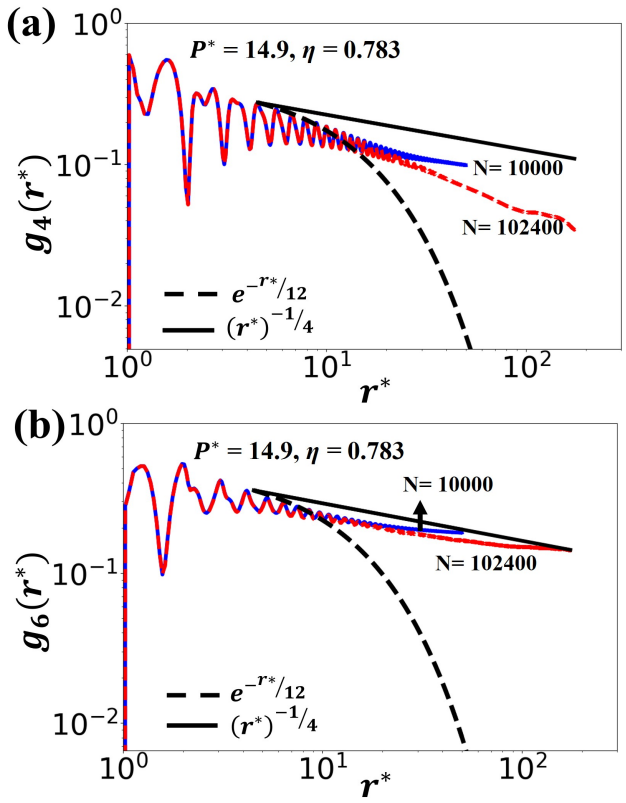

Fig. 5 (color online). Bond orientational order functions $g_4(r^*)$ (a) and $g_6(r^*)$ (b) for the M region of equimolar disks+squares mixture with $\xi = 1.1$ for N= 10000 and 102400 particles. The dashed and solid lines indicate algebraic and exponential decays with exponent $-1/4$ and $-1/12$, respectively.

Figures 6a and 6d (inset) show configurations of the M region and the two-phase coexistence state at P^*= 14.9 and η= 0.783, and P^*= 16.5 and η = 0.80, respectively. The clusters of six-fold and four-fold ordered domains are shown by coloring the particles based on the local values of Φ_6 (Fig. 6b) and Φ_4 (Fig. 6c). For the M region, the coloring reveals a complementary correlation between the disk-rich regions with high six-fold clusters and square-rich regions with high four-fold ordered clusters, that are randomly distributed throughout the simulated domain. We also detected regions of RB order formed by squares with high local values of Φ_6. To test that the M region is not just a system that has become kinetically arrested *en route* to macro-phase separation, we simulated a system started at a state of complete phase separation of squares and disks at P^*=14.9, and confirmed that the macro-domains gradually disintegrated to form M micro-domains. Movie 2 in the SI shows this process for an equimolar mixture with N= 39712 particles. Overall, our analysis indicates that the M region indeed comprises near-critical configurations having a heterogeneous

microstructure resembling a *"mosaic"* of different ordered micro-domains which locally resemble *tetratic/RB-like* and *hexatic-like* regions.

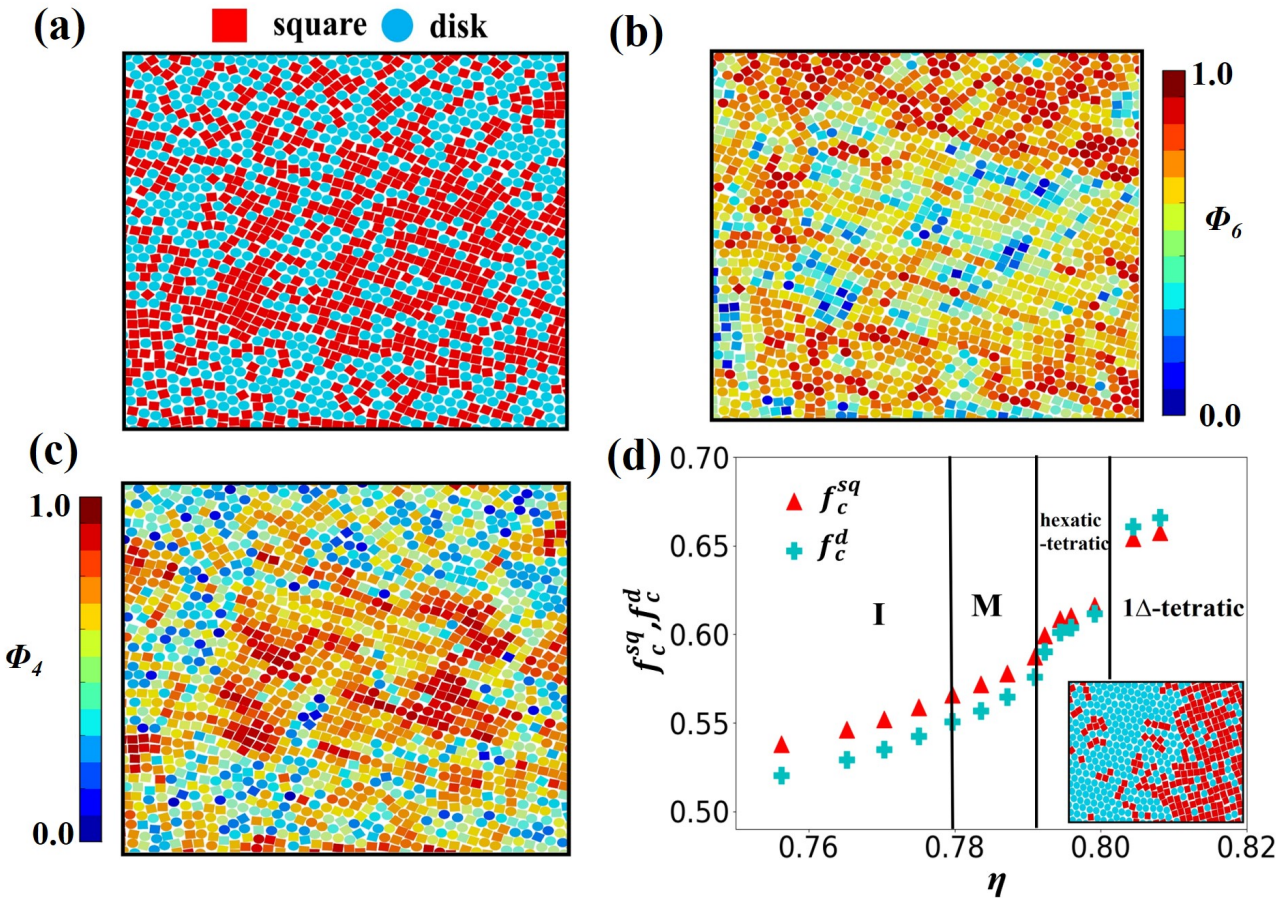

Fig. 6 (color online). Local bond orientational and compositional order for the equimolar disks+squares mixture with $\xi = 1.1$ and $N = 10000$. (a)-(c) correspond to the M region at $\eta = 0.783$ where the particles are colored based on type (a) and the local values of Φ_6 (b) and Φ_4 (c). Each snapshot represents a ~1/10th section of the entire simulation box. (d) Approximate phase boundaries and local composition parameters, f_c^{sq} and f_c^d, as a function of area fraction, η. The inset shows a representative snapshot of two-phase coexistence state at $\eta = 0.8$. I = isotropic phase, M = mosaic region.

To understand the mechanism associated with the onset of the M region from the I phase, we computed the local composition parameters, f_c^{sq} and f_c^d to detect the correlation between the local compositional heterogeneity and the presence of ordered domains formed by squares and disks (see Fig. 6d). Parameters f_c^{sq} and f_c^d are the average fraction of the like-shaped nearest neighbors

to a square and disk, respectively (normalized such that particles with all like-shaped neighbors corresponds to 1). For the I phase, the average values of both f_c^{sq} and f_c^d are close to a well-mixed value of 0.5, reflecting the overall equimolar composition. Upon compression, both f_c^{sq} and f_c^d increase gradually in the M region (for $\eta > 0.78$), and then more steeply as the hexatic-tetratic two-phase separated region is reached ($\eta > 0.791$). The loss of the particles' local compositional mixing observed in the M region compared to the I phase, reveals that the entropic bonding [59,60], which favors contacts between like-shaped particles, becomes sufficiently strong to seed the formation of disk-rich six-fold and square-rich four-fold micro-domains. The grain boundaries around these micro-domains contain particles with both f_c^{sq} and f_c^d values close to 0.5, which can be viewed as compositional *"defects"* contributing to the structural disorder in the M region. The migration of these defects was monitored at $\eta = 0.783$ using *"pseudo dynamic"* Monte Carlo simulations in the *NVT* ensemble. Movie 3 in the SI shows that, although the migration of these defects is restricted to the grain boundary regions, their compositions decorrelate much faster compared to particles inside ordered domains (see Fig. S8c Sec. VI of SI). This suggests that both the growth of ordered M domains from the I state, and the slow restructuring of the M domain patterns would be mediated by the accrual of local rearrangements at the grain boundaries. The compositional defects observed in the M region are expected to be correlated with the topological defects typically observed in the melting transition of two-dimensional solids.

The growth of the six-fold and four-fold ordered domains as the M region is entered from the I phase was tracked by performing a cluster analysis. The protocol used to identify such clusters is described in the SI Sec. IV. The fraction of particles belonging to the largest four-fold and the largest six-fold clusters increased as the system enters the M region (see Figs. 7a and 7b). In the M region, these largest *n*-fold (where $n = 4$ or 6) cluster tends to form a loose, interconnected network that is randomly distributed percolating the simulation box as shown in the snapshots in Fig 7. While we expect the *n*-fold clusters to form a percolating network at the critical point, we observed that the six-fold clusters also percolated the sample in the M region, likely due to the finite size effects. In the I phase in contrast, the largest *n*-fold clusters are isolated and much smaller. We also observed a higher fraction of particles in the six-fold clusters compared to the four-fold clusters as the local RB order formed in the square-rich region also contributes to the six-fold symmetry (see Sec.VI Fig.S9 in SI). The fractal nature of the six-fold and four-fold clusters is consistent with a continuous phase transition. Figure 8 shows the relative orientational angle

between the largest six-fold and the largest four-fold clusters in selected states of the I phase, M and (hexatic-tetratic) two-phase regions (see Sec. IV in SI). As the system follows the sequence I → M → (hexatic-tetratic) two-phase regions, the orientational correlation between the neighboring six-fold and four-fold ordered clusters increases ($|\theta_6-\theta_4| \rightarrow 0$), consistent with the growing correlation length of bond-ordering in the whole system and indicative of the preferential alignment of the particles between the square-rich and disk-rich domains.

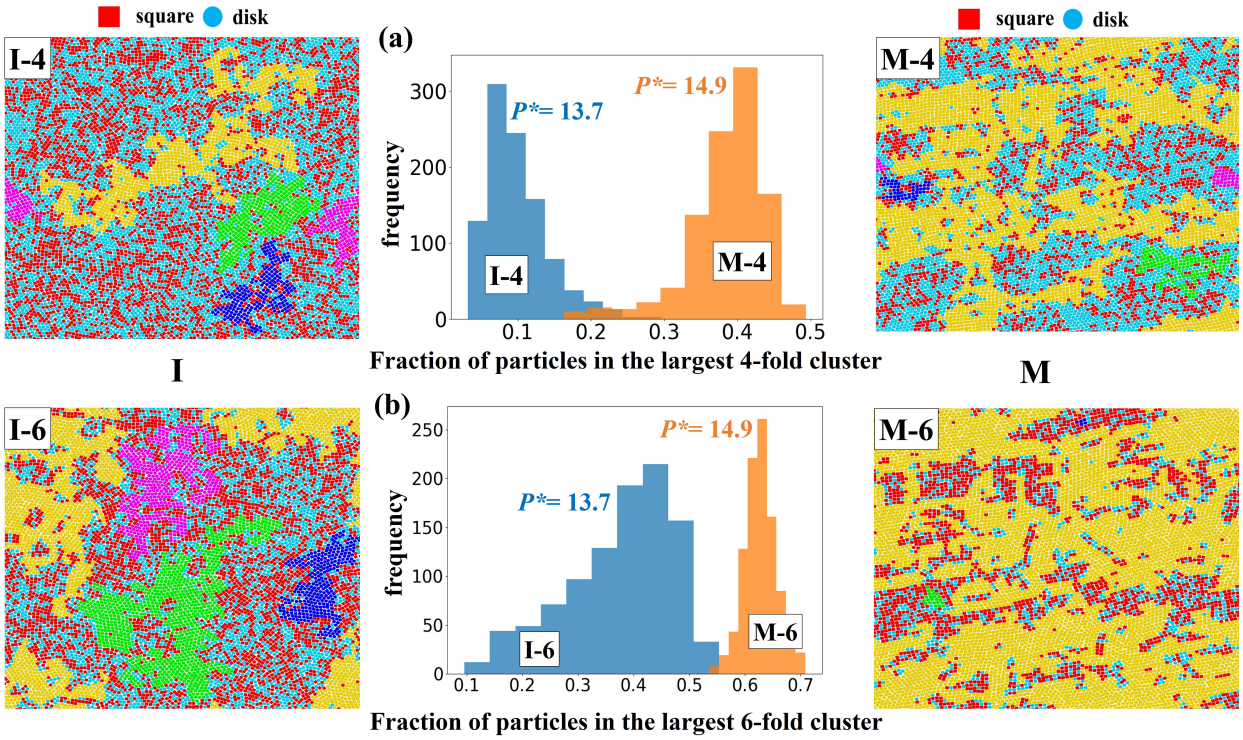

Fig. 7 (color online). Growth of the four-fold and six-fold ordered domains for the equimolar disks+squares mixture with $\xi = 1.1$ and $N = 10000$ for I phase (at $P^*=13.7$) and the M region (at $P^*=14.9$). Distribution function of the fraction of particles belonging to the largest four-fold (a) and six-fold (b) clusters. Representative snapshots for the I and M configurations are labelled as I-4 and M-4 for four-fold clusters and I-6 and M-6 for six-fold clusters. The particles belonging to the first, second, third, and fourth largest clusters are colored in yellow, green, magenta and blue, respectively.

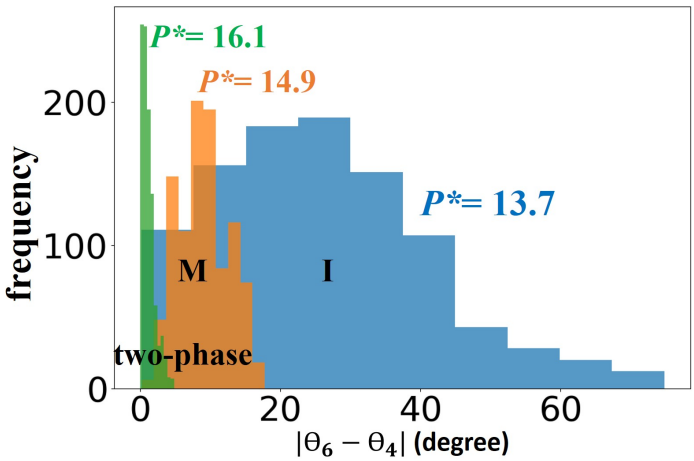

Fig. 8 Relative orientational angle between the largest six-fold and the largest four-fold clusters for representative I (blue), M (orange), and two-phase (green) states. I = isotropic phase, M = mosaic region.

Unlike most other near-critical point phenomena described in the literature, particle energetics play no role in the underlying phase transition and it is hence instructive to discuss entropy effects. The overall mixing entropy in the M region, while lower than that in the I phase (where nearly ideal mixing occurs), must be significant. Indeed, while limited mixing happens at the length scale of individual particles inside clusters (as in the solid solutions) and at the grain boundaries, *'random'* mixing also occurs at the length scale of the six-fold and four-fold ordered clusters due to the local compositional fluctuations near the critical point that scale in proportion to the correlation length of the ordered clusters. The result is a system with transient but well-defined *micro*-phase segregated regions which is quite distinct to the *macro*-phase segregated state observed above the critical pressure.

In our athermal system, pressure and the associated pressure×volume (*PV)* "enthalpic" contribution to the free energy, act as the knob that controls the strength of the packing entropy that optimizes local particle arrangements and its interplay with mixing entropy. At low pressure, the local compositions are uncorrelated and the interparticle coupling is weak, with a neighboring site to a square or disk being indistinctly occupied by another square or disk (quasi random distribution). At higher pressure, compositional correlations and coupling is strong due to the loss in mixing entropy, favoring the formation of denser, orientationally aligned six-fold (disk-rich)

and four-fold (square-rich) clusters that minimize the free energy by enhancing $P\Delta V < 0$ effects. Note that a more efficient packing is typically associated with a gain in vibrational motion (and associated entropy) of individual particles. The M region observed in this work thus engenders when there is a close balance between the packing entropy favoring optimal packing of the particles and the mixing entropy favoring contact between unlike particles.

We posit then that the domain clustering of M configurations engenders when, at a suitable range of compositions and densities, the two competing entropic forces, namely, entropic bonding favoring like-particle contacts and mixing entropy favoring random contacts, are in such a close balance that are able to coexist by attaining a *"compromise"* state exhibiting both segregated like-particle domains and random mixing of those domains. As the M region is compressed to a higher density, the entropic cost of unlike contacts overpowers any gain in mixing entropy, leading (upon crossing a critical point) to the phase separation of the components into disk-rich and square-rich ordered phases. Conceptually, the $\mathrm{I} \rightarrow \mathrm{M} \rightarrow$ two-solid-phase progression with pressure for an equimolar mixture could be seen as the coarsening in the correlation length of the ordered domains, which goes from being very short ranged (I phase), to mesoscopic (M region) to macroscopic (two-phase state).

To underscore the significance of the optimal component size ratio, ξ, we also simulated phase diagrams for other ξ values for the disk+square mixture. We varied the ξ values by $\pm$ 27% from the representative optimal value of 1.1 so that the associated ΔF_x values are significantly higher than those in the relatively flat region for $1.04 < \xi < 1.2$ (see Fig. 1). Specifically, Fig. 9 shows results for $\xi = 0.8$ and 1.4 for which, unlike the $\xi = 1.1$ case in Fig. 2, no M region was detected. In both cases, the stability region of the hexatic phase is much narrower compared to the $\xi = 1.1$ case. Furthermore, while for the $\xi = 1.1$ case both the disk-rich and square-rich phases and solid solution regions are large and comparable in size (giving the phase diagram a symmetric look), those regions become very asymmetric for the other ξ values; i.e., the hexatic and 1Δ regions are small, especially for the $\xi = 0.8$ case. These results clearly show that a system with a (near) optimal choice of ξ promotes the stability of ordered phases with substitutional disorder over wider ranges of composition and pressure and, by construction of ΔF_x [see Eq. (1)], it does so in a way that *both* pure-component ordered phases are similarly represented (see Sec. VII). Arguably, the microscopic substitutional symmetry favored by a minimal ΔF_x gets translated into a macroscopic

symmetry in the substitutionally disordered solids and partially ordered phases in the phase diagram.

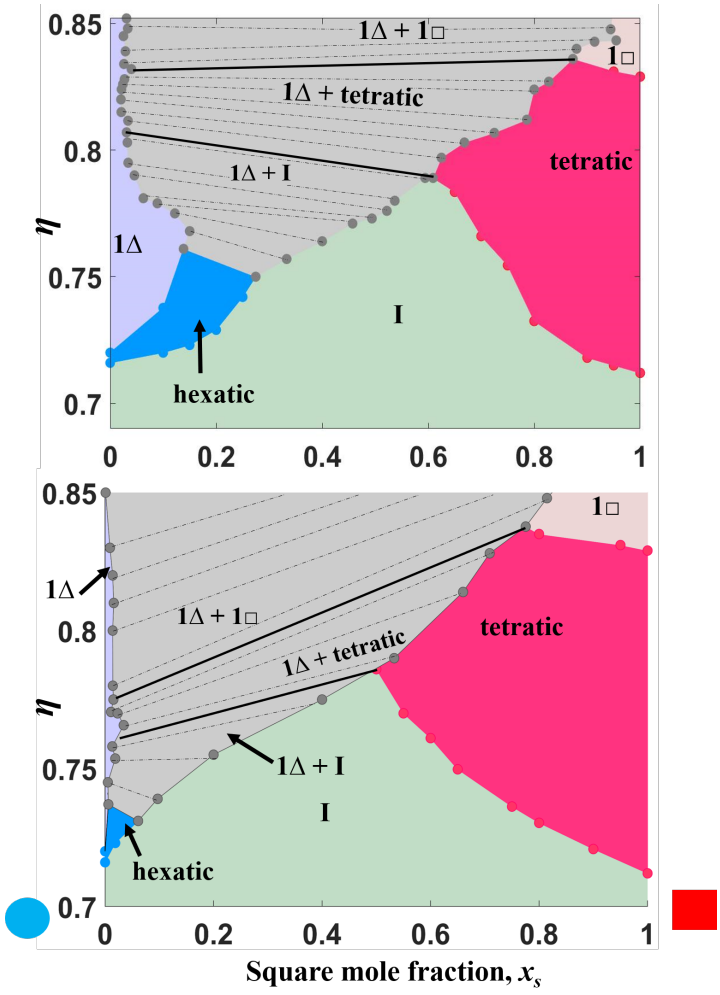

Fig. 9 (color online). Area fraction-composition phase diagrams for disks (diameter σ) and squares (side edge a) with different size ratios, $\xi = \sigma/a$. Top: $\xi = 0.8$, bottom: $\xi = 1.4$. The tie lines in the two-phase regions are shown as dashed lines. 1Δ = triangular solid, 1□ = square solid, and I = isotropic phase.

IV. Final Remarks and Outlook

In summary, for the crystal-symmetry incompatible mixture of disk+squares with optimized size ratio ($\xi = 1.1$), we mapped the pressure-composition phase diagram which revealed broad ranges of compositions and pressures where the hexagonal solid and hexatic phase (favored by disks) and square solid and tetratic phase (favored by squares) form. Moreover, we identified a distinctive M

region that resides near the critical point for the hexatic-tetratic phase coexistence and is characterized by randomly distributed, persistent micro-domains corresponding to four-fold and six-fold regions. In contrast, for the crystal-symmetry compatible mixture of disks and hexagons with optimized size ratio (ξ = 1.82), the corresponding phase diagram shows that a 1Δ solid solution and the hexatic phase form over the entire range of compositions.

While the competition between 1Δ/hexatic and 1□/tetratic ordering is not uncommon in 2D or quasi-2D systems, structures resembling those in the M region have only been seen under very restrictive conditions. For example, cuboctahedral nanoparticles pinned at 2D fluid-fluid interfaces have been observed to transition from a hexagonal to a square lattice only as transient, non-equilibrium states (e.g., as surface ligands are removed and particles bond through their <100> facets) [61]. 2D simulations of hard rounded squares [62] of a particular degree of roundedness have predicted the formation of a *"polycrystalline"* phase with a patchy-domain structure loosely reminiscent of configurations of the M region. Through the rounding of square-corners, such a system provides a physical interpolation (in a single-component system) between disks and squares to reach a state where the entropic tendencies towards the formation of hexagonal and square lattices are in close balance, like that achieved in the M region by our disks+squares binary mixture.

Structures from the M region found in the disks+squares mixture could display interesting optical phenomenon such as critical opalescence since the near-critical point fluctuations of the local composition cause the sizes of both four-fold and six-fold symmetry domains to fluctuate over large length scales. Alternatively, the dual structural symmetry observed in the M region could be leveraged for specialty applications, e.g., to fabricate a synthetic Chameleon skin [63], optical switches [64], or optical biosensors [65]. Indeed, M configurations consist of pervading seeds of both hexatic and tetratic phases, whose global order could then be readily biased (through a suitable external field) to switch between one phase and the other. The methods used and principles unveiled in this work should be general and applicable to many other athermal mixtures.

Acknowledgement

Funding support from NSF award CBET-1907369 is gratefully acknowledged. The authors thank Yangyang Sun, Unmukt Gupta, Srinath Ranya and Isabela Quintela Matos for useful exchanges and to Abhishek Sharma and Ankita Mukhtyar for valuable suggestions on the cluster analysis.

References:

[1] J. Henzie, M. Grünwald, A. Widmer-Cooper, P. L. Geissler, and P. Yang, Nat. Mater. **11**, 131 (2012).

[2] D. Seo, C. P. Ji, and H. Song, J. Am. Chem. Soc. **128**, 46 (2006).

[3] S. J. Penterman, A. Singh, W. R. Zipfel, and C. M. Liddell Watson, Adv. Opt. Mater. **2**, 11 (2014).

[4] S. Badaire, C. Cottin-Bizonne, J. W. Woody, A. Yang, and A. D. Stroock, J. Am. Chem. Soc. **129**, 1 (2007).

[5] C. J. Hernandez and T. G. Mason, J. Phys. Chem. C **111**, 12 (2007).

[6] U. Agarwal and F. A. Escobedo, Nat. Mater. **10**, 230 (2011).

[7] S. C. Glotzer and M. J. Solomon, Nat. Mater. **6**, 557 (2007).

[8] Y. Min, M. Akbulut, K. Kristiansen, Y. Golan, and J. Israelachvili, Nat. Mater. **7**, 527 (2008).

[9] Y. F. Lim, J. J. Choi, and T. Hanrath, J. Nanomater. **2012**, 393160 (2012).

[10] G. Von Freymann, A. Ledermann, M. Thiel, I. Staude, S. Essig, K. Busch, and M. Wegener, Adv. Funct. Mater. **20**, 1038 (2010).

[11] A. V. Kabashin, P. Evans, S. Pastkovsky, W. Hendren, G. A. Wurtz, R. Atkinson, R. Pollard, V. A. Podolskiy, and A. V. Zayats, Nat. Mater. **8**, 867 (2009).

[12] C. Novo, A. M. Funston, and P. Mulvaney, Nat. Nanotechnol. **3**, 598 (2008).

[13] C. R. Henry, Catal. Letters **145**, 731 (2015).

[14] Z. Y. Zhou, N. Tian, J. T. Li, I. Broadwell, and S. G. Sun, Chem. Soc. Rev. **40**, 4167 (2011).

[15] J. H. Conway, Y. Jiao, and S. Torquato, Proc. Natl. Acad. Sci. U. S. A. **108**, 11009 (2011).

[16] G. Bautista-Carbajal, P. Gurin, S. Varga, and G. Odriozola, Sci. Rep. **8**, 8886 (2018).

[17] S. Torquato and Y. Jiao, Nature **460**, 876 (2009).

[18] M. R. Khadilkar and F. A. Escobedo, Soft Matter **12**, 1506 (2016).

[19] P. F. Damasceno, M. Engel, and S. C. Glotzer, ACS Nano **6**, 609 (2012).

[20] E. G. Teich, G. Van Anders, D. Klotsa, J. Dshemuchadse, and S. C. Glotzer, Proc. Natl. Acad. Sci. U. S. A. **113**, E669 (2016).

[21] J. A. Anderson, J. Antonaglia, J. A. Millan, M. Engel, and S. C. Glotzer, Phys. Rev. X **7**, 021001 (2017).

[22] X. Ye, J. E. Collins, Y. Kang, J. Chen, D. T. N. Chen, A. G. Yodh, and C. B. Murray, Proc. Natl. Acad. Sci. U. S. A. **107**, 22430 (2010).

[23] E. K. Riley and C. M. Liddell, Langmuir **26**, 11648 (2010).

[24] W. J. Baumgardner, K. Whitham, and T. Hanrath, Nano Lett. **13**, 3225 (2013).

[25] W. H. Evers, B. Goris, S. Bals, M. Casavola, J. De Graaf, R. Van Roij, M. Dijkstra, and D. Vanmaekelbergh, Nano Lett. **13**, 2317 (2013).

[26] B. Liu, T. H. Besseling, M. Hermes, A. F. Demirörs, A. Imhof, and A. Van Blaaderen, Nat. Commun. **5**, 3092 (2014).

[27] W. H. Evers, J. M. Schins, M. Aerts, A. Kulkarni, P. Capiod, M. Berthe, B. Grandidier, C. Delerue, H. S. J. Van Der Zant, C. Van Overbeek, J. L. Peters, D. Vanmaekelbergh, and L. D. A. Siebbeles, Nat. Commun. **6**, 8195 (2015).

[28] M. Danek, K. F. Jensen, C. B. Murray, and M. G. Bawendi, Chem. Mater. **8**, 173 (1996).

[29] B. I. Halperin and D. R. Nelson, Phys. Rev. Lett. **41**, 155702 (1978).

[30] A. P. Young, Phys. Rev. B **19**, 1855 (1979).

[31] D. R. Nelson and B. I. Halperin, Phys. Rev. B **19**, 2457 (1979).

[32] J. M. kosterlitz and D. J. Thouless, J. Phys. C Solid State Phys. **6**, 1181 (1973).

[33] E. P. Bernard and W. Krauth, Phys. Rev. Lett. **107**, 155702 (2011).

[34] J. A. Millan, D. Ortiz, G. Van Anders, and S. C. Glotzer, ACS Nano **8**, 2918 (2014).

[35] J. Russo and N. B. Wilding, Phys. Rev. Lett. **119**, 115702 (2017).

[36] A. Buhot and W. Krauth, Phys. Rev. E - Stat. Physics, Plasmas, Fluids, Relat. Interdiscip. Top. **59**, 2939 (1999).

[37] R. L. C. Vink, J. Horbach, and K. Binder, Phys. Rev. E - Stat. Nonlinear, Soft Matter Phys. **71**, 011401 (2005).

[38] B. Trefz, J. T. Siebert, T. Speck, K. Binder, and P. Virnau, J. Chem. Phys. **146**, 074901 (2017).

[39] J. Stenhammar, R. Wittkowski, D. Marenduzzo, and M. E. Cates, Phys. Rev. Lett. **114**, 018301 (2015).

[40] M. Han, J. Yan, S. Granick, and E. Luijten, Proc. Natl. Acad. Sci. U. S. A. **114**, 29 (2017).

[41] P. A. Rice and H. M. McConnell, Proc. Natl. Acad. Sci. **86**, 17 (1989).

[42] S. L. Keller and H. M. Mc Connell, Phys. Rev. Lett. **82**, 1602 (1999).

[43] K. Zhao, R. Bruinsma, and T. G. Mason, Proc. Natl. Acad. Sci. **108**, 7 (2011).

[44] F. A. Escobedo, J. Chem. Phys. **146**, 134508 (2017).

[45] M. R. Khadilkar and F. A. Escobedo, Phys. Rev. Lett. **113**, 165504 (2014).

[46] M. Mazars, Epl **84**, 55002 (2008).

[47] M. R. Khadilkar, U. Agarwal, and F. A. Escobedo, Soft Matter **9**, 11557 (2013).

[48] E. G. Gilbert, D. W. Johnson, and S. S. Keerthi, IEEE J. Robot. Autom. **4**, 193 (1988).

[49] P. J. Schneider and D. H. Eberly, *Geometric Tools for Computer Graphics* (Elsevier, 2003).

[50] H. Weber, D. Marx, and K. Binder, Phys. Rev. B **51**, 14636 (1995).

[51] M. Engel, J. A. Anderson, S. C. Glotzer, M. Isobe, E. P. Bernard, and W. Krauth, Phys. Rev. E - Stat. Nonlinear, Soft Matter Phys. **87**, 042134 (2013).

[52] N. B. Wilding, Phys. Rev. E **52**, 602 (1995).

[53] A. D. Bruce and N. B. Wilding, Phys. Rev. Lett. **68**, 193 (1992).

[54] L. B. Stutzman, F. A. Escobedo, and J. W. Tester, Mol. Simul. **44**, 147 (2018).

[55] N. B. Wilding, J. Phys. Condens. Matter **9**, 585 (1997).

[56] W. T. Góźdź, J. Chem. Phys. **119**, 3309 (2003).

[57] W. T. Góźdź and A. Ciach, Condens. Matter Phys. **19**, 1 (2016).

[58] M. Casiulis, M. Tarzia, L. F. Cugliandolo, and O. Dauchot, J. Chem. Phys. **150**, 154501 (2019).

[59] G. Van Anders, N. K. Ahmed, R. Smith, M. Engel, and S. C. Glotzer, ACS Nano **8**, 1 (2014).

[60] G. Van Anders, D. Klotsa, N. K. Ahmed, M. Engel, and S. C. Glotzer, Proc. Natl. Acad. Sci. U. S. A. **111**, 45 (2014).

[61] K. Whitham and T. Hanrath, J. Phys. Chem. Lett. **8**, 2623 (2017).

[62] C. Avendaño and F. A. Escobedo, Soft Matter **8**, 4675 (2012).

[63] J. Teyssier, S. V. Saenko, D. Van Der Marel, and M. C. Milinkovitch, Nat. Commun. **6**, 1 (2015).

[64] J. Ge, Y. Hu, T. Zhang, T. Huynh, and Y. Yin, Langmuir **24**, 3671 (2008).

[65] P. Damborský, J. Švitel, and J. Katrlík, Essays Biochem. **60**, 91 (2016).